Theory of rotating electrohydrodynamic flows in a liquid film

E. V. Shiryaeva*
Department of Mathematics, Mechanics and Computer Science, Southern Federal University, 344090 Rostov-on-Don, Russia

V. A. Vladimirov†
Department of Mathematics, York University, York YO10 5DD, United Kingdom

M. Yu. Zhukov‡
Department of Mathematics, Mechanics and Computer Science, Southern Federal University, 344090 Rostov-on-Don, Russia

(Received 20 February 2009; revised manuscript received 15 July 2009; published 16 October 2009)

The mathematical model of rotating electrohydrodynamic flows in a thin suspended liquid film is proposed and studied. The flows are driven by the given difference of potentials in one direction and constant external electric field $\boldsymbol{E}_{\text{out}}$ in another direction in the plane of a film. To derive the model, we employ the spatial averaging over the normal coordinate to a film that leads to the average Reynolds stress that is proportional to $|\boldsymbol{E}_{\text{out}}|^3$. This stress generates tangential velocity in the vicinity of the edges of a film that, in turn, causes the rotational motion of a liquid. The proposed model is used to explain the experimental observations of the *liquid film motor*.

DOI: 10.1103/PhysRevE.80.041603 PACS number(s): 68.15.+e, 47.32.Ef, 47.57.jd

I. INTRODUCTION

The paper is devoted to the electrohydrodynamics (EHD) of a thin suspended liquid film where the flows are driven by constant external electric field applied at the edges of a film. This research was inspired by the laboratory experiments [1–3] where various rotating flows have been observed in a water cell placed inside a plane capacitor. The ability of a constant electric field to generate and to maintain rotating flows looks so striking that the authors [1–3] called this effect a *liquid film motor*, emphasizing that it represents a new type of engine. Simultaneously, they denied the possibility of generation such a flow by the edge effects and proposed the heuristic explanation based on the changing of orientation of water molecular dipoles due to a strong electric field. In contrast, we show that an averaged rotating flow in a film can be generated by the edge effects, so the appearance of rotating flows can be explained within the classical EHD theory. More precisely, we show that the jump of an electric field across a water-dielectric interface can produce (due to the electrokinetic effects) the tangential velocity of a fluid that, in turn, can maintain a steady rotating flow in a film. The related physical mechanism is simple and clear. The field of the capacitor creates the opposite electric charges in the fluid near the interface boundaries. Then the action of the electric field (related to the potential differences between the electrodes) creates the rotating flow.

Naturally, our final model for the averaged flows is two-dimensional (a plane one); however, the tangential velocity at the side boundaries is caused by the Reynolds stresses that are obtained by the averaging over the film thickness of an original three-dimensional flow. The resulting tangential velocity has the magnitude $O(h^4)$, where $2h$ is the film thickness. An intense EHD rotating flow in the whole film takes place only in the restricted domain of governing parameters. According to our theory, the ratio between the spatial scales of a flow domain plays a crucial role: rotating flows can exist only in moderately thin films and cannot appear in the flow domains where all spatial sizes are of similar order as well as in too thin films. For example, the tangential velocity ~ 1 cm/s appears for the following parameters: the strength of the capacitor electric field ~ 30 kV/m, the difference of electrolysis potentials ~ 20 V, the film thickness $\sim 0.1-0.3$ cm, and the film surface size ~ 1 cm. To build our model, we employ only two basic physical assumptions: the absence of the pondermotive forces and the absence of the surface stresses. All other assumptions, we use represent the mathematical adjustments of various physical requirements (such as the rest of the film as a whole, the no-leak for both liquid and concentrations, the conditions for the electric potential and its derivatives at the boundary, etc.) to the considered geometry. The main general result of our paper is the demonstration of the fact that classical EHD effects (such as the electrokinetic phenomena), that are small in ordinary conditions, can play the key part in microscales. Such a revaluation of classical EHD effects may play important part in the developments of microfluidics and in the creation of microdevices.

In our mathematical modeling, we essentially use the results [4–9] on the analytical and numerical studies of the EHD flows with the gradient of conductivity, the method of depth average, and the effective asymptotic procedure for the EHD equations of multicomponent mixtures. In the averaged equations derived in [4–8], one can observe the terms describing the Taylor-Aris dispersion and the Reynolds stresses; however, the latter are neglected since they are small for the chosen intervals of parameters and negligible for the studied phenomena. It is also useful that in [7], one can find the comparison between the mathematical models of the different levels of approximation.

*shir@ns.math.rsu.ru
†vv500@york.ac.uk
‡zhuk@ns.math.rsu.ru

We can also mention closely related to our studies papers [10–14] which consider EHD flows in thin liquid films or in liquid layers with interfaces [15], describes the appearance of vortex rings due to reactions near an electrode, and [16] presents a rotating EHD flow in a smectic medium. The role of the interface boundary conditions in EHD is well known from classical papers [17–19]. The important paper [20] shows that an *electrical double layer* (ED) can allow the slip in the boundary conditions between a liquid and a solid. The papers [21–26] are devoted to the influence of the inhomogeneous electrical charge of microchannel boundaries on EHD flows. Other papers [27–31] consider various theories of the EDL, including so-called extremal regimes. The survey of modern EDL theories can be found in [32].

The attention to various flows in micro- and nanoscales has increased greatly during the last few years. For example, the main parts of recent surveys [33,34] are devoted to EHD processes in microchannels [35–40] and deal with various flows in microchannels including the flows caused by the injection of a fluid. This attention is strongly stimulated by the creation of the microfabricated fluid devices for the separation or micromixing of multicomponent mixtures [41–46], the electromicropumps [47], etc. These new devices are known as parts of the *lab-on-a-chip technology*. In this booming research area, the mathematical models can help to understand and describe the microprocesses, to develop experimental methods, and to construct microchips.

In the paper, first we present the rigorous asymptotic theory and then we study the relation of our results to the experiments [1–3]. Section II contains the original and dimensionless governing EHD equations and boundary conditions as well as the list of the dimensionless variables used. In Sec. III, we present the plane-averaged EHD equations and the boundary conditions that are involved in the description of rotating flows. How we derive these equations is explained fully and systematically in Appendix A. In Sec. IV, we present the simplified asymptotic model describing the flow near the side boundaries of a film. The results of this section allow us to estimate the impact of Reynolds stresses on the near-wall flows and to derive the formula that links a flow velocity with the strength of the electric field in a capacitor. These questions are also considered in Appendix B. In Sec. V and Appendix C, we present the simplified equations and boundary conditions for averaged flows. The obtained analytical solution allows us to predict the qualitative structure of the flows. The main purpose of Secs. III–V is to give the asymptotic evaluation of the main parameters. This evaluation allows us to split the solution of our problem into two parts: the deriving of the boundary conditions based on EDL and the computations of a rotating flow. Section VI contains the results of computational experiments for the selected set of parameters. Here we describe the rotating flows in a square film by the presenting of their velocity fields. In addition, we characterize the differential rotation of the liquid by three different parameters: by the averaged vorticity, by the averaged ratio v_θ/r, and by the period of rotation of a passive scalar admixture. We also consider the flows in rectangular films and the flows in a film with smothered angles. Finally, we compare the flows with the no-slip and free-surface boundary conditions. The detailed discussion is given in Sec. VII.

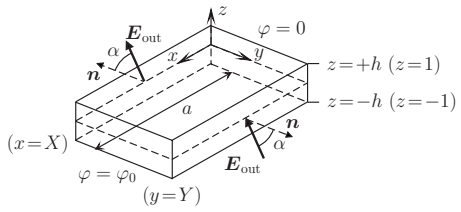

FIG. 1. A sketch of thin film.

II. BASIC EQUATIONS

A rectangular thin liquid film with fixed-plane free surfaces $z=\pm h$ is considered in Cartesian coordinates (x,y,z) (Fig. 1). The gravity and the surface tension are absent. An electric field can be conveniently split into two parts. The first part is due to the constant electric potentials $\varphi=0$ and $\varphi=\varphi_0$ on the boundaries $x=0$ and $x=X$, so the constant difference of potentials is applied in the direction x. The second part is a constant external electric field $\boldsymbol{E}_{\text{out}}$ that is prescribed at the boundaries $y=0$ and $y=Y$. The vector $\boldsymbol{E}_{\text{out}}$ lies in the plane $z=$const and α is the angle between this vector and y axis.

The dimensional system of governing equations describing the EHD processes in multicomponent mixtures is well known (see, e.g., [4,7,48]). Here, we first present all equations of this system and then describe the notations used. The Navier-Stokes equations include the additional terms for the pondermotive force $(1/2)\boldsymbol{E}^2\nabla\varepsilon$ and the force $q\boldsymbol{E}$ exerted on a charge

$$\rho\frac{\partial \boldsymbol{v}}{\partial t}+\rho\boldsymbol{v}\cdot\nabla\boldsymbol{v}=-\nabla p+\nu\rho\Delta\boldsymbol{v}-\frac{1}{2}\rho\boldsymbol{E}^2\nabla\varepsilon+q\boldsymbol{E}. \quad (1)$$

The continuity equation

$$\operatorname{div}\boldsymbol{v}=0. \quad (2)$$

The Poisson-Boltzmann equation

$$\operatorname{div}(\varepsilon\boldsymbol{E})=q. \quad (3)$$

The charge of the multicomponent medium consists of the charges of components and the electric field has the potential

$$\rho_e=F\sum_k e_k c_k, \quad \boldsymbol{E}=-\nabla\varphi. \quad (4)$$

The mass transfer is described by the balance equations that do not contain chemical reactions (the Nernst-Plank equations without source terms)

$$\frac{\partial c_k}{\partial t}+\boldsymbol{v}\cdot\nabla c_k+\operatorname{div}\boldsymbol{i}_k=0, \quad (5)$$

$$\boldsymbol{i}_k=-D_k\nabla c_k+e_k\gamma_k c_k\boldsymbol{E}. \quad (6)$$

Here, $\boldsymbol{v}$ is velocity (m/s), p is pressure $(\mathrm{N/m^2})$, ρ is liquid density $(\mathrm{kg/m^3})$, q is charge density $(\mathrm{C/m^3})$, φ is electric potential (V), $\boldsymbol{E}$ is electric field strength (V/m), c_k is molar concentration for the kth component of mixture $(\mathrm{mol/m^3})$, $\boldsymbol{i}_k$ is density fluxes for concentrations $[\mathrm{mol/(m^2\ s)}]$, ν is kinematic viscosity $(\mathrm{m^2/s})$, D_k is diffusivity for the components of a mixture $(\mathrm{m^2/s})$, e_k are the electric charges of compo-

nents (in the units of electron charge), ε is the solution permittivity [$\varepsilon=\varepsilon_r\varepsilon_0$, where ε_r is relative permittivity and ε_0 is absolute permittivity, C/(V m)], γ_k are electric mobilities [$m^2/(V\ s)$], and F is Faraday constant (C/mol).

A. Scaling

For the dimensionless variables, we use the following characteristic values of parameters:

$$[x,y]=a_*,\quad [z]=h_*,\quad [t]=\mathcal{T}_*,\quad [u,v]=\frac{a_*}{\mathcal{T}_*},$$

$$[w]=\frac{h_*}{\mathcal{T}_*},\quad [c_k]=\mathcal{C}_*,\quad [E]=\mathcal{E}_*,\quad [\varphi]=\mathcal{E}_*a_*,$$

$$[q]=F_*\mathcal{C}_*,\quad [p]=F_*\mathcal{C}_*\mathcal{E}_*a_*\delta^2,$$

$$\gamma=\frac{F_*\mathcal{E}_*a_*}{R_*T_*},\quad \mathcal{T}_*^2=\frac{\rho_*a_*}{F_*\mathcal{C}_*\mathcal{E}_*\delta^2},\quad \delta^2=\frac{h_*^2}{a_*^2}. \tag{7}$$

Here, a_* is the characteristic length in the plane of the film, h_* and δ are the dimensional and dimensionless half thicknesses of the film, $\mathcal{T}_*$ and $\mathcal{C}_*$ are characteristic time and molar concentration, $F_*\mathcal{C}_*$ is the characteristic charge density, R_* is the universal gas constant, T_* is the absolute temperature of a solution, and $a_*\mathcal{E}_*$ is the characteristic difference of electric potentials in the x direction. The dimensional values of kinematic viscosity ν_*, diffusion coefficients D_k^*, and dielectric permittivity ε_* are linked to their dimensionless counterparts as

$$\nu=\frac{\nu_*\mathcal{T}_*}{a_*^2},\quad D_k=\frac{D_k^*\mathcal{T}_*}{a_*^2},\quad \varepsilon=\frac{\varepsilon_*\mathcal{E}_*}{a_*F_*\mathcal{C}_*}. \tag{8}$$

The use of dimensionless parameters (viscosity, diffusivity, etc.) instead of conventional scaling numbers (Reynolds number, Peclet number, etc.) is more convenient for our purposes since they allow us to see which physical effects participate into a certain process. The connections between the introduced parameters and the scaling numbers are apparent

$$\mathrm{Re}=\frac{1}{\nu},\quad \mathrm{Pe}_k=\frac{1}{D_k}.$$

B. Dimensionless equations

The dimensions of all involved variables are listed after Eqs. (1)–(6). For brevity, we use the same notations for dimensionless variables as for their dimensional counterparts. This usage can cause confusion where both types of variables are used simultaneously; in these cases, the dimensional variables are asteriated.

We take the dielectric permittivity ε=const that leads to the vanishing of the pondermotive force $(1/2)\nabla\varepsilon(\nabla\varphi)^2=0$. Hence, the dimensionless system of governing equations describing the EHD flows of multicomponent fluid is

$$\delta^2\frac{d\boldsymbol{u}}{dt}=-\delta^2\nabla_0 p+\delta^2\nu\Delta_0\boldsymbol{u}+\nu\partial_{zz}\boldsymbol{u}-q\nabla_0\varphi, \tag{9}$$

$$\delta^4\frac{dw}{dt}=-\delta^2\partial_z p+\delta^4\nu\Delta_0 w+\nu\delta^2\partial_{zz}w-q\partial_z\varphi, \tag{10}$$

$$\mathrm{div}_0\,\boldsymbol{u}+\partial_z w=0, \tag{11}$$

$$\varepsilon(\delta^2\Delta_0\varphi+\partial_{zz}\varphi)=-\delta^2 q,\quad q=\sum_k e_k c_k, \tag{12}$$

$$\delta^2\frac{dc_k}{dt}+\delta^2\,\mathrm{div}_0\,\boldsymbol{i}_k+\partial_z I_k=0, \tag{13}$$

$$\boldsymbol{i}_k=-D_k(\nabla_0 c_k+e_k\gamma c_k\nabla_0\varphi), \tag{14}$$

$$I_k=-D_k(\partial_z c_k+e_k\gamma c_k\partial_z\varphi),$$

$$\boldsymbol{\Gamma}=(\sigma_{13},\sigma_{23},0)=\nu(\partial_z\boldsymbol{u}+\delta^2\nabla_0 w),$$

$$\frac{d}{dt}=\partial_t+\boldsymbol{u}\cdot\nabla_0+w\partial_z,\quad \nabla_0=(\partial_x,\partial_y),\quad \Delta_0=\partial_{xx}+\partial_{yy}. \tag{15}$$

Here, $\boldsymbol{v}=(\boldsymbol{u},w)$ is the velocity and $\boldsymbol{u}=(u,v)$ is its (x,y) projection, $\boldsymbol{i}_k$ and I_k are the planar and transversal density fluxes for concentrations, the parameter γ characterizes the ratio between the transports of concentrations by an electric field and by diffusion, 2δ is the dimensionless film thickness, and $\boldsymbol{\Gamma}$ is the tangential stress vector that is expressed via the components σ_{13} and σ_{23} of a viscous stress tensor.

The used method of the introducing of dimensionless variables [see Eq. (7)] allows us to write separately the variables and equations that describe the processes in the plane of a film, such as the Eq. (9) for the plane velocity $\boldsymbol{u}$ and the Eqs. (13) and (14) for the plane transfer of concentrations c_k.

C. Boundary conditions

On the film boundaries $z=\pm 1$, we accept the no-leak condition for velocity

$$w|_{z=\pm1}=0, \tag{16}$$

the tangent stress-free condition, that with the use of Eq. (16) takes form

$$\boldsymbol{\Gamma}|_{z=\pm1}=\nu(\partial_z\boldsymbol{u}+\delta^2\nabla_0 w)|_{z=\pm1}=\nu\partial_z\boldsymbol{u}|_{z=\pm1}=0, \tag{17}$$

the no-leak conditions for concentrations

$$I_k|_{z=\pm1}=0, \tag{18}$$

and the vanishing of the normal electric current

$$\partial_z\varphi|_{z=\pm1}=0. \tag{19}$$

For the deriving of the averaged model in Sec. III and in Appendix A, we use the governing Eqs. (9)–(15). In our averaging procedure, we only use the boundary conditions (16)–(19). The additional boundary conditions (defined for the averaged equations) are given in Sec. III.

III. AVERAGING ACROSS A FILM

The main part of the employed averaging procedure is the same as in [4–8]. The operation of averaging is defined as

$$\bar{f}(x,y,t) = \frac{1}{2}\int_{-1}^{1} f(x,y,z,t)dz, \quad \tilde{f} \equiv f - \bar{f}. \tag{20}$$

We decompose the solution of Eqs. (9)–(19) into the series

$$\{\boldsymbol{u},w,p,q,c_k,\varphi\} = \sum_{m=0} \{\boldsymbol{u}^m,w^m,p^m,q^m,c_k^m,\varphi^m\}\delta^{2m}$$
$$= \sum_{m=0} \{\bar{\boldsymbol{u}}^m,\bar{w}^m,\bar{p}^m,\bar{q}^m,\bar{c}_k^m,\bar{\varphi}^m\}\delta^{2m}$$
$$+ \sum_{m=0} \{\tilde{\boldsymbol{u}}^m,\tilde{w}^m,\tilde{p}^m,\tilde{q}^m,\tilde{c}_k^m,\tilde{\varphi}^m\}\delta^{2m}. \tag{21}$$

The averaging of the governing Eqs. (9)–(14), which takes into account the boundary conditions (16)–(19) and the decomposition into the small parameter δ^2, first yields $\bar{q}=\bar{q}^0+O(\delta^2)$, $\bar{\varphi}=\bar{\varphi}^0+O(\delta^2)$, $\bar{c}_k=\bar{c}_k^0+O(\delta^2)$, $\tilde{\varphi}^0=0$, $\tilde{c}_k^0=0$, and $\tilde{q}^0=0$ and then leads to the expressions for $\tilde{\boldsymbol{u}}^0$, $\tilde{w}^0$ $\tilde{c}_k^1$. The averaged plane equations that retain the terms $O(\delta^2)$ are (for details, see Appendix A)

$$\delta^2\frac{d_0\bar{\boldsymbol{u}}}{dt} + \beta\nabla_0(\boldsymbol{U}\otimes\boldsymbol{U}) = -\delta^2\nabla_0\bar{p} + \delta^2\nu\Delta_0\bar{\boldsymbol{u}} - \nu\boldsymbol{U}, \tag{22}$$

$$\mathrm{div}_0\,\bar{\boldsymbol{u}} = 0, \tag{23}$$

$$\varepsilon\Delta_0\bar{\varphi} = -\bar{q}, \quad \bar{q} = \sum_k e_k\bar{c}_k, \tag{24}$$

$$\frac{d_0\bar{c}_k}{dt} - \alpha_k\delta^2\,\mathrm{div}_0[\boldsymbol{U}(\boldsymbol{U}\cdot\nabla_0\bar{c}_k)] + \mathrm{div}_0\,\bar{\boldsymbol{i}}_k = 0,$$

$$\bar{\boldsymbol{i}}_k = -D_k(\nabla_0\bar{c}_k + e_k\gamma\bar{c}_k\nabla_0\bar{\varphi}), \tag{25}$$

$$\frac{d_0}{dt} \equiv \partial_t + \bar{\boldsymbol{u}}\cdot\nabla_0, \quad \nu\boldsymbol{U} \equiv \bar{q}\nabla_0\bar{\varphi},$$

$$\beta \equiv \frac{\delta^2}{45}, \quad \alpha_k \equiv \frac{4}{945D_k}, \tag{26}$$

where $(\boldsymbol{U}\otimes\boldsymbol{U})$ denotes a tensorial product. We emphasize that after this averaging, δ must be treated as a regular independent parameter of the problem, jointly with ν, ε, D_k, etc.

Boundary conditions for two-dimensional domain

For the Eqs. (22)–(26), we prescribe the boundary conditions for the averaged fields $\bar{\boldsymbol{u}}$, $\bar{c}_k$, and $\bar{\varphi}$ on the side boundaries $x=0$, X and $y=0$, Y (Figs. 1 and 2). The boundaries $y=0$ and $y=Y$ represent the interfaces between two dielectric materials: the liquid of dielectric permittivity ε and the outside medium of dielectric permittivity $\varepsilon_{\mathrm{out}}$. These boundaries are insulators (not electrodes), hence we require the continuity of the normal components of electric induction [48,49]

$$\varepsilon(\boldsymbol{n}\cdot\nabla_0\bar{\varphi}) = \varepsilon_{\mathrm{out}}(\boldsymbol{n}\cdot\boldsymbol{E}_{\mathrm{out}}), \quad y=0,Y,$$

where $\boldsymbol{n}$ is the normal unit vector to the boundary. Since vector $\boldsymbol{E}_{\mathrm{out}}$ lies in the plane $z=$const and has the angle α with y axis, we have

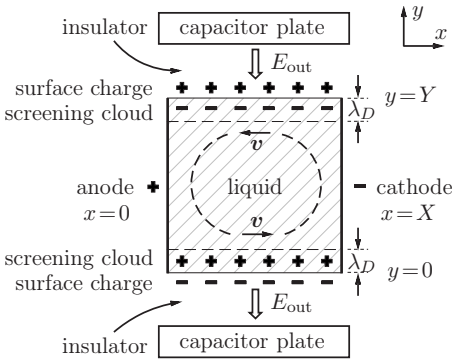

FIG. 2. The physical mechanism of rotation. The capacitor field creates the opposite electric charges in the fluid near the interface boundaries $y=0$, Y. Then the action of electric field related to electrodes (applied in x direction) generates the rotating flow.

$$\frac{\partial\bar{\varphi}}{\partial\boldsymbol{n}} = \pm E_0, \quad y=0,\ Y; \quad E_0 = \frac{\varepsilon_{\mathrm{out}}}{\varepsilon}|\boldsymbol{E}_{\mathrm{out}}|\cos\alpha, \tag{27}$$

where the sign "–" corresponds to the boundary $y=0$ (Fig. 1). The conditions of zero concentration fluxes at $y=0$, Y are

$$\bar{\boldsymbol{i}}_k\cdot\boldsymbol{n} = 0, \quad y=0,\ Y. \tag{28}$$

The fixed difference between the electric potentials at $x=0$ and $x=X$ is given as

$$\bar{\varphi} = 0, \quad x=0; \quad \bar{\varphi} = \varphi_0, \quad x=X. \tag{29}$$

For all edge boundaries $x=0$, X and $y=0$, Y, we require the no-leak of a liquid

$$\bar{u}|_{x=0,X} = 0, \quad \bar{v}|_{y=0,Y} = 0 \tag{30}$$

and the analog of Helmholtz-Smoluchowski slip condition

$$\bar{\boldsymbol{u}}\cdot\boldsymbol{\tau}|_{y=0,Y} = -\mathcal{R}\nabla_0\bar{\varphi}\cdot\boldsymbol{\tau}|_{y=0,Y}, \tag{31}$$

$$\bar{\boldsymbol{u}}\cdot\boldsymbol{\tau}|_{x=0,X} = -\mathcal{R}\nabla_0\bar{\varphi}\cdot\boldsymbol{\tau}|_{x=0,X}, \tag{32}$$

where $\boldsymbol{\tau}$ is a unit tangent vector to the boundary and $\mathcal{R}$ is the coefficient defined in Sec. IV. By virtue of Eq. (29), the boundary conditions (32) for $x=0$, X take the no-slip form

$$\bar{v}|_{x=0,X} = 0. \tag{33}$$

The prescription of tangential velocity (31) at the boundaries $y=0$, Y is justified in Sec. IV where we show that $\mathcal{R}\sim E_0^3$. This derivation is performed from the Eq. (22) that contains the averaged Reynolds stresses

$$\beta\nabla_0(\boldsymbol{U}\otimes\boldsymbol{U}) \equiv \beta(\boldsymbol{U}\cdot\nabla_0\boldsymbol{U} + \boldsymbol{U}\,\mathrm{div}_0\,\boldsymbol{U}), \tag{34}$$

which define $\mathcal{R}$ for certain intervals of parameters ν, δ, ε, etc.

The derivation of Eqs. (22)–(26) is given in Appendix A. Here we mention only that the boundary conditions (16)–(19) at $z=\pm 1$ play a central part in this derivation. It is also well known that the use of the spatial averaging only does not allow producing the closed systems of equations; for its closure, one has to employ some additional hypotheses. As such a hypothesis, we impose the condition $\bar{w}^0=0$

that is natural from the physical viewpoint. The equations similar to Eqs. (22)–(26) have been obtained in [4–8] (and in other papers cited there) and devoted to the studies of the EHD flows with the spatially nonuniform conductivity. These papers also contain the decomposition into power series and even the term similar to Eq. (34). However, the key difference with our paper is that this term is small for the physical parameters considered in [4–8], so it is naturally neglected.

IV. FLOWS NEAR BOUNDARIES

The problem (22)–(34) can be split into the sequence of two problems: (i) the calculation of $\mathcal{R}$ in Eq. (31) and (ii) the finding of the averaged velocity field $\bar{\boldsymbol{u}}$ and the averaged potential $\bar{\varphi}$. In order to evaluate $\mathcal{R}$, we assume that the mixture is electroneutral everywhere except the vicinities of the boundaries $y=0$, Y. In these vicinities, we build the boundary-layer solution that leads to a good estimation for $\mathcal{R}$. The detailed studies of the related double layers (the Gouy-Chapman layer or diffusion layer, the Stern layer, etc.) can be found in [20,22–25,28–32], where nonlinear and steric effects are taken into account along with linear electrokinetic effects. From the mathematical viewpoint, different EDL theories are aimed to formulate and justify different boundary conditions for the related boundary layers. The main question is how to choose the mutual positions of a physical boundary and an interface between the regions with positive and negative charges.

The appearance of a tangential velocity near the boundaries is rather obvious from the physical viewpoint. It can be explained as an electrokinetic effect (electro-osmosis); the correspondent theory was introduced by Smolukhowski in 1905 and then developed in the papers we quoted above. This theory is based on the fact that the surface charges of the insulator induce the equal but opposite in sign charges inside the liquid which form the Debye screening layers of the characteristic thickness λ_D^* near the insulator boundaries. Then the electrical field related to the electrodes generates the tangential velocity that has opposite directions near $y=0$ and $y=Y$. These opposite velocities, in turn, generate the rotation of a liquid (see Fig. 2).

To study this phenomenon in more details, we consider the vicinity of the boundary $y=0$ (the case $y=Y$ is similar) and look for the steady solution of the problem (22)–(30) in the form

$$\bar{\boldsymbol{u}} = (\bar{u}(y),0), \quad \bar{c}_k = \bar{c}_k(y), \quad \bar{\varphi} = \Phi(y) + Ex, \tag{35}$$

where E is the constant tangential component of the electric field in the vicinity of $y=0$. For simplicity, we neglect the terms $\alpha_k \delta^2 \boldsymbol{U}(\boldsymbol{U}\cdot\nabla_0 \bar{c}_k)$ in Eq. (25). The form (35) of a solution is commonly used in the EDL theory for the deriving of the relation between the strength of an electric field and the flow velocity at a boundary (see, e.g., [50]). The requirement $E=$const is not essential. It is used only for the simplification of calculations; physically it corresponds to the "local" consideration of a short boundary segment. When the required relation is derived, E is allowed to be dependent on x and y.

The integration of Eq. (25) with the boundary conditions (28) yields

$$\bar{c}_k(y) = c_{Bk} e^{-e_k \gamma \Phi(y)}, \quad \bar{q}(y) = \sum_k e_k c_{Bk} e^{-e_k \gamma \Phi(y)}, \tag{36}$$

where c_{Bk} are the constants representing concentrations for the equilibrium Boltzmann distributions. We restrict ourselves with the case when the mixture is electroneutral, only two kinds of ions are present (for example, H^+ and OH^- for water) and the equilibrium Boltzmann distribution is valid

$$c_{B1} = c_{B2} \overset{\text{def}}{=} c_B, \quad z_1 = 1, \quad z_2 = -1. \tag{37}$$

The Poisson-Boltzmann Eq. (24) takes the form

$$\lambda^2 \partial_{yy}\theta = \sinh\,\theta, \quad \theta(y) = \gamma\Phi(y), \tag{38}$$

where λ_D^* and λ are the Debye length and the relative Debye length (see also Fig. 2)

$$\lambda^2 = \frac{\varepsilon}{2\gamma c_B} = \frac{(\lambda_D^*)^2}{a_*^2} \ll 1, \quad (\lambda_D^*)^2 = \frac{\varepsilon_* R_* T_*}{2 c_B^* F_*^2}. \tag{39}$$

In the vicinity of $y=0$, the boundary-layer variable is introduced as $y=\lambda\eta$ (similarly, at $y=Y$, the change of variable is $y=Y+\lambda\eta$).

In more precise terms, the considered boundary-layer solution represents the so-called "penetrating boundary layer" [51]. In this case, the original equations and the boundary-layer equations coincide and $\lambda \ll 1$ is not required for the obtaining of a solution. Instead of looking for the boundary-layer solution decaying at infinity, one can use the symmetry with respect to $y=Y/2$; the result will remain the same. Nevertheless, our further consideration follows the path that is more transparent from the physical viewpoint. Equation (38) takes form

$$\partial_{\eta\eta}\theta(\eta) = \sinh\,\theta(\eta). \tag{40}$$

Its integration with the boundary condition (27) for $\Phi(0)$ yields

$$\theta(0) = -\theta_0, \quad \gamma\Phi(0) = -\theta_0, \tag{41}$$

where

$$\theta_0 = \ln(1 + \mathbb{E}^2 + \mathbb{E}\sqrt{2+\mathbb{E}^2}), \quad \mathbb{E}^2 = \frac{\gamma\varepsilon}{4c_B} E_0^2.$$

The expression for $\Phi(Y)$ is similar to Eq. (41)

$$\theta(0) = \theta_0, \quad \gamma\Phi(Y) = \theta_0.$$

The boundaries $y=0$ and $y=Y$ represent the different plates of a capacitor, therefore the opposite signs of potential Φ are apparent. The calculation of $\beta\nabla_0(\boldsymbol{U}\otimes\boldsymbol{U})$ with the use of Eqs. (26), (34), and (35) yields

$$\beta\nabla_0(\boldsymbol{U}\otimes\boldsymbol{U}) = \frac{\beta}{\nu^2}[E\partial_y(\bar{q}^2\partial_y\Phi),\ \partial_y(\bar{q}\partial_y\Phi)^2], \tag{42}$$

where the right-hand side (written in components) allows us to integrate the Eq. (22) with the additional condition $u(\infty)=0$. This condition means that the flow arising near the boundary must decay at large distance from this boundary, i.e., the distributions of the horizontal component u and po-

tential Φ are of a boundary-layer type (for more details, see Appendix B)

$$\frac{\beta E\varepsilon^2}{\nu^2\lambda^4\gamma^3}\int_{\infty}^{\eta}(\partial_{\eta\eta}\theta)^2\partial_\eta\theta d\eta=\delta^2\nu u(\eta)+\frac{\varepsilon E\theta(\eta)}{\gamma}. \quad (43)$$

For the obtaining of the boundary condition (31) and defining $\mathcal{R}$, we evaluate the integral at $\eta=0$,

$$\int_{\infty}^{0}(\partial_{\eta\eta}\theta)^2\partial_\eta\theta d\eta=\int_0^{\theta(0)}\sinh^2\theta d\theta=\frac{1}{2}(\sinh\theta_0\cosh\theta_0-\theta_0).$$

Taking into account that $E=-(\boldsymbol{\tau}\cdot\nabla_0\varphi)_{y=0}$ and comparing Eq. (43) to Eq. (31), we obtain (the case $y=Y$ is similar)

$$\mathcal{R}=\mathcal{R}_3+\mathcal{R}_1,\quad \mathcal{R}_1=\pm\frac{\varepsilon}{\delta^2\nu\gamma}\theta_0,$$

$$\mathcal{R}_3=\pm\frac{2c_B^2\beta}{\delta^2\nu^3\gamma}(\sinh\theta_0\cosh\theta_0-\theta_0), \quad (44)$$

where different signs correspond to $y=0$ and $y=Y$. After the use of series decomposition, we can replace the expression (45) for $\mathcal{R}_3$ by

$$\mathcal{R}_3\approx\pm\frac{8c_B^2\beta}{3\delta^2\nu^3\gamma}\sqrt{2}\mathbb{E}^3,\quad \mathbb{E}\le 0.6. \quad (45)$$

The error of the above replacement is below 5% for $\mathbb{E}\le 0.6$ (for the real parameters of Sec. VI, the value $\mathbb{E}\approx 0.01$, hence the relative error of this replacement is 0.0001). In order to avoid misunderstanding, we should mention that the calculated value of $\mathcal{R}$ (31) represents only a rough estimation; to obtain, it we accept that the Eq. (25) is steady and we can neglect the Taylor-Aris dispersion. Moreover, in Eq. (35), we assume that $E=$const on the boundaries $y=0$, Y that is not true; later on, we consider $E=E(x)$ [see Eq. (51)]. In spite of these simplifying assumptions, the results of this section show that Reynolds stresses $\beta\nabla_0(\boldsymbol{U}\otimes\boldsymbol{U})$ can crucially participate to the generation of the tangential velocity [of order $O(E_0^3)$] at the side boundary of a film.

V. FLOW IN A THIN FILM

In order to describe the flow in a thin film, we use the simplified version of the Eqs. (22)–(26), where we accept that the mixture is electroneutral ($\bar{q}=0$) everywhere but at the vicinities of the boundaries. It allows us to eliminate from the equations all terms proportional to $\boldsymbol{U}$, taking them into account only in the boundary conditions (see Sec. IV). The problem describing the averaged velocity $\bar{\boldsymbol{u}}=(\bar{u},\bar{v})$ and the averaged potential $\bar{\varphi}$ is

$$\partial_t\bar{\boldsymbol{u}}+\bar{\boldsymbol{u}}\cdot\nabla_0\bar{\boldsymbol{u}}=-\nabla_0\bar{p}+\nu\Delta_0\bar{\boldsymbol{u}},\quad \mathrm{div}_0\bar{\boldsymbol{u}}=0, \quad (46)$$

$$\Delta_0\bar{\varphi}=0, \quad (47)$$

where Eq. (47) corresponds to the continuity equation for an electric current in the case of constant conductivity and equal diffusion coefficients D_k (see Appendix C); Eq. (47) is not the Poisson-Boltzmann Eq. (24) that expresses the potential via the charge that was used in Sec. IV, the formal coincidence of these equations should not cause misunderstanding. We solve Eqs. (46) and (47) in the rectangular domain $\mathcal{D}=\{0\le x\le X,\ 0\le y\le Y\}$ with the boundary conditions (27), (29), (30), (32), and (33)

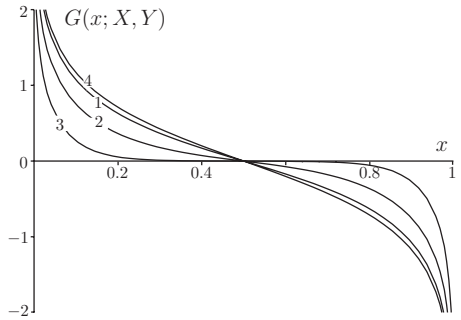

FIG. 3. The function $G(x;X,Y)$ for $X=1$ and the different values of Y: (1) $Y=1$, (2) $Y=0.5$, (3) $Y=0.2$, and (4) $Y=2$.

$$\bar{\boldsymbol{u}}|_{x=0,X}=0,\quad \bar{v}|_{y=0,Y}=0, \quad (48)$$

$$\bar{u}|_{y=0,Y}=-\mathcal{R}\bar{\varphi}_x|_{y=0,Y},\quad \mathcal{R}=\mathcal{R}_1(E_0)+\mathcal{R}_3(E_0), \quad (49)$$

$$\bar{\varphi}|_{x=0}=0,\quad \bar{\varphi}|_{x=X}=\varphi_0,\quad \bar{\varphi}_y|_{y=0,Y}=E_0. \quad (50)$$

The value $\mathcal{R}$ is given by Eq. (45) and the value of $\mathcal{R}$ essentially depends on E_0 as it follows from the expressions:

$$\mathcal{R}_1\approx\pm\frac{\varepsilon\sqrt{2\varepsilon}}{2\delta^2\nu\sqrt{\gamma c_B}}E_0,\quad \mathcal{R}_3\approx\pm\frac{\beta\varepsilon\sqrt{2\gamma\varepsilon c_B}}{3\delta^2\nu^3}E_0^3.$$

The problem Eqs. (47) and (50) has the analytic solution that can be presented as Fourier's series. For the further use, we give the following formula (where the sign "+" corresponds to $y=0$)

$$\bar{\varphi}_x|_{y=0,Y}=\frac{\varphi_0}{X}\pm E_0G(x;X,Y),$$

$$G(x;X,Y)=\frac{4}{\pi}\sum_{k=0}^{\infty}\frac{\tanh\frac{(2k+1)\pi Y}{2X}}{(2k+1)}\cos(2k+1)\frac{\pi x}{X}. \quad (51)$$

The computed graphs of $G(x;X,Y)$ for the different values of X and Y are shown in Fig. 3.

It is apparent that for the fixed X and Y, the sign of $\bar{\varphi}_x|_{y=0,Y}$ [and hence the tangential velocity $\bar{u}|_{y=0,Y}$ given by Eq. (49)] depends on the relation between the parameters φ_0, E_0. For example, for $X=Y=1$ and $\varphi_0/X=E_0$, the velocity $u<0$ on the part of the boundary $\{0<x\lesssim 0.1, y=0\}$ and $u>0$ on the rest of it $\{0.1\lesssim x<1,\ y=0\}$. The graphs of Fig. 3 allow us to give the qualitative explanation of the flow structures; in particular it is used in Sec. VI for the explanation of Fig. 4.

The numerical solution of the problem (46)–(50) is presented below with the use of the stream function $\bar{\psi}$ which is defined by the equations

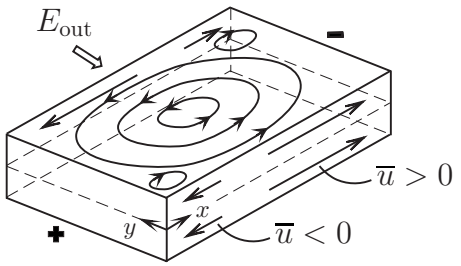

FIG. 4. The sketch of a rotating flow in the film.

$$\bar{u} = \bar{\psi}_y, \quad \bar{v} = -\bar{\psi}_x, \quad \omega \equiv \bar{v}_x - \bar{u}_y,$$

$$\Delta\bar{\psi} = \bar{u}_y - \bar{v}_x = -\omega, \quad \bar{\psi}|_{x=0,X} = \bar{\psi}|_{y=0,Y} = 0.$$

Case when the electrodes represent free boundaries

At the electrodes $x=0$, X, we have accepted the no-slip boundary conditions (48) for $\bar{\boldsymbol{u}}$. It is also interesting to consider the different case when the electrodes represent free boundaries, which require the tangential no-stress condition

$$\bar{u}|_{x=0,X} = 0, \quad \bar{v}_x|_{x=0,X} = 0.$$

VI. NUMERICAL RESULTS

We solve the Navier-Stokes Eqs. (46) with the prescribed tangential velocity and the no-leak condition at $y=0$, Y and the no-slip condition at the rest of the boundary (48) and (49) by the employment of the standard projection algorithm [52,53] and the finite element method. The numerical setting is based on the package FREEFEM++ [54] with the use of adaptive grids. The formula (51) for $\bar{\varphi}_x|_{y=0,Y}$ is not efficient due to its singularities at $x=0$, X; therefore taking into account the singularities of derivatives near the vertices, we also find $\bar{\varphi}$ [Eqs. (47) and (50)] numerically.

The formulated problem is rather simple, however, the qualitative properties of its solution strongly depend on the relation between the parameters φ_0, E_0, X, and Y. As we have already mentioned, the direction of the tangential velocity on the boundaries $y=0$, Y is defined by Eq. (51) (Fig. 3): the velocity is positive on one part of each boundary and is negative on its remaining part (Fig. 4). The particular velocity distribution depends mainly on the ratio φ_0/E_0.

It is apparent that this tangential velocity causes the rotational motion of a large scale. Some additional smaller vortices can appear in the regions adjacent to the parts of the boundary, where the tangential velocity has the opposite sign (Fig. 4).

It is instructive to express dimensionless parameters in terms of dimensional ones with the use of Eqs. (7), (8), and (45)

$$\frac{a_*}{\mathcal{T}_*}\mathcal{R}_1 = -\frac{\varepsilon_*\mathcal{E}_*^2}{\rho_*\nu_*}\lambda_D^* E_0,$$

$$\frac{a_*}{\mathcal{T}_*}\mathcal{R}_3 \approx \frac{F_* c_B^* \varepsilon_* \mathcal{E}_*^3}{135\rho_*^2\nu_*^3}\left(\frac{2\varepsilon_*\mathcal{E}_*^2}{R_* T_* c_B^*}\right)^{1/2} E_0^3 h_*^4,$$

$$\lambda_D^* = \left(\frac{\varepsilon_* R_* T_*}{2c_B^* F_*^2}\right)^{1/2}, \quad \mathcal{T}_* = \frac{a_*}{h_*}\sqrt{\frac{\rho_* a_*}{F_* c_B^* \mathcal{E}_*}},$$

$$\nu = \frac{\nu_* \mathcal{T}_*}{a_*^2}, \quad E_0 = \frac{\varepsilon_{\text{out}}^*}{\varepsilon_*}\frac{E_{\text{out}}^*}{\mathcal{E}_*}, \quad \varphi_0 = \frac{\varphi_0^*}{a_*\mathcal{E}_*}. \tag{52}$$

We perform our computations for the experimental values of *parameters for a liquid film motor* taken from [1–3]; all used values are listed in Tables I–III. It is apparent that the velocity $(a_*/\mathcal{T}_*)\mathcal{R}_1$ (that is similar to the classic electroosmosis) is significantly less than the tangential velocity on the boundary $(a_*/\mathcal{T}_*)\mathcal{R}_3$ that appears due to the averaging over the film thickness. Therefore in the computations, we

TABLE I. Dimensional parameters.

Symbol	Description	Value
φ_0^*	Difference of potentials	20 V
a_*	Length	10^{-2} m
E_{out}^*	Electric intensity	30000 V/m
ν_*	Kinematic viscosity	10^{-6} m^2/s
ε_0^*	Absolute permittivity	8.85×10^{-12} C/(V m)
ε_*	Water permittivity	$78.3\varepsilon_0^*$
$\varepsilon_{\text{out}}^*$	Air permittivity	$1.0\varepsilon_0^*$
ρ_*	Water density	10^3 kg/m^3
$\mathcal{C}_*=c_B^*$	Ion concentration	10^{-4} mol/m^3
F_*	Faraday constant	9.65×10^4 C/mol
R_*	Universal gas constant	8.3 J/(mol K)
T_*	Absolute temperature	293 K

TABLE II. Characteristic scales.

Symbol	Description	Value
$\mathcal{E}_*$	Electric strengths scale	2000 V/m
$\mathcal{T}_*$	Time scale	7.7×10^{-2} s
$a_*/\mathcal{T}_*$	Velocity scale	0.13 m/s
$1/\mathcal{T}_*$	Angular velocity scale	12.99 Rad/s
$\mathcal{R}_3(a_*/\mathcal{T}_*)$	Tangent velocity scale	3×10^{-2} m/s
$\mathcal{R}_1(a_*/\mathcal{T}_*)$	Tangent velocity scale	0.5×10^{-6} m/s
λ_D^*	Debye's length	0.95×10^{-6} m
$h_*=\delta a_*$	Half height	0.29×10^{-2} m

TABLE III. Dimensionless parameters.

Figure	E_0	$-\varphi_0$	δ	$\nu\times10^4$	$\mathcal{R}_3$	$\mathcal{R}_3/E_0^3$	X	Y
5–10, 12, 14–17	0.19	1.0	0.29	7.7	0.235	33.42	1.0	1.0
11	0.19	1.0	0.29	7.7	0.235	33.42	1.0	0.5
13	0.19	0.1	0.29	7.7	0.235	33.42	1.0	1.0

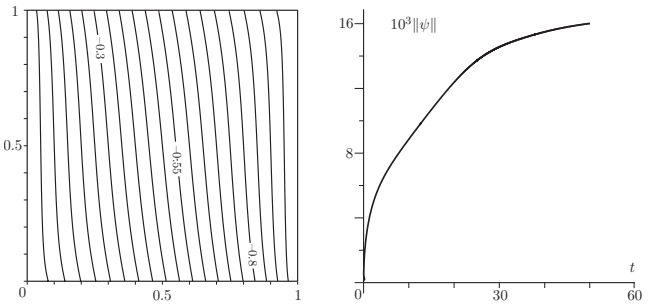

FIG. 5. The isolines of the potential $\bar{\varphi}(x,y)$ (left) and $\|\bar{\psi}(\cdot,t)\|$.

have not taken $\mathcal{R}_1$ into account. One can see that $\delta^2 \approx 0.09$; it gives us a sufficient ground to treat δ^2 as a small parameter and to use Eqs. (22)–(26).

A. Flows in square domain

Let us show the results of computations in a square and in a rectangle. The left part of Fig. 5 shows the isolines for the potential $\bar{\varphi}(x,y)$ with the step 0.05. Figure 6 demonstrates the streamlines of $\bar{\psi}(x,y,t)$ with the step 0.002 at the instants $t=10$ (≈ 0.77 s) and $t=30$ (≈ 2.31 s).

The isolines of the velocity field $\bar{\boldsymbol{u}}(x,y,t)$ at $t=30$ are given in Fig. 7. After $t=30$, the flow is practically steady; for the additional control of the relaxation to a steady state, we calculate the mean-square norm $\|\bar{\psi}(\cdot,t)\|$ (Fig. 5).

More detailed discussion of the computational results is given in Sec. VII. Here, we just mention that Fig. 6 shows the initial appearance of two corotating vortices. Later on, these two vortices merge into a single vortex that in the whole domain represents an almost steady rotating flow. For the considered parameters, the transition (relaxation) to the final steady flow takes around 2 s.

It is more convenient to describe rotating flows in polar coordinates (r,θ) with the radial v_r and azimuthal v_θ velocity components

$$v_r = \bar{u}\cos\theta + \bar{v}\sin\theta, \quad v_\theta = -\bar{u}\sin\theta + \bar{v}\cos\theta,$$

$$x = 0.5 + r\cos\theta, \quad y = 0.5 + r\sin\theta.$$

The isolines of $v_r(x,y,t)$ and $v_\theta(x,y,t)$ (with the step 0.02) along with the additional isoline $v_r(x,y,t)=0.01$, all at

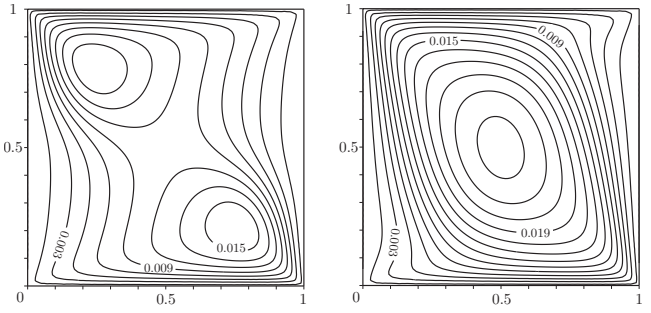

FIG. 6. The streamlines of $\bar{\psi}(x,y,t)$ for $t=10$ (≈ 0.77 s) and $t=30$ (≈ 2.31 s).

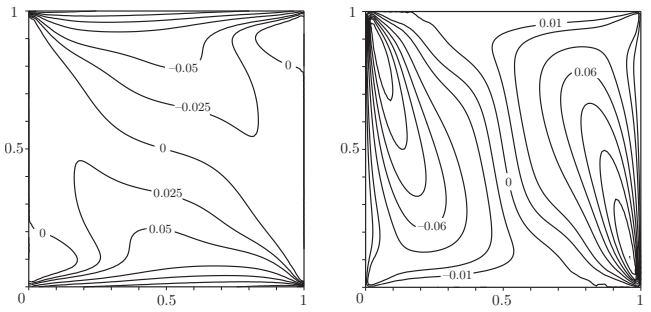

FIG. 7. The isolines of $\bar{u}(x,y,t)$ (left) and $\bar{v}(x,y,t)$ at $t=30$.

$t=30$, are shown in Fig. 8. It is worth to notice that $v_\theta(x,y,t) \geq 0$ that means *all fluids* are rotating anticlockwise.

Figures 7 and 8 show that the velocity field is rather complex for rather simple geometry of streamlines $\bar{\psi}(x,y,t)$ given in Fig. 6. The isolines of ω (which denotes the z component of vorticity rot $\bar{\boldsymbol{u}}$) are shown in Fig. 9; they are presented with the step 0.1 along with the additional isolines 0.35, 0.375, and 0.45.

The vortex core with the value of vorticity $\omega \approx 0.4$ is shown in Fig. 9 as the dashed circle $0<r<0.25$. In addition in Fig. 9, we give the graphs of $\omega(r,\theta_m,t)$ for $\theta_m = m\pi/4$, $m=0$, 1, 2, 3, and 4 and $t=30$ in polar coordinates (r,θ). The presence of an elliptic vortex core is also visible from the distribution of azimuthal velocity component v_θ (Fig. 8).

The averaged angular velocity Ω_0 appears as the result of the averaging of vorticity over the flow domain $\mathcal{D}=\{0\leq x\leq X,\ 0\leq y\leq Y\}$,

$$\Omega_0 = \frac{1}{2}\langle\omega\rangle = \frac{1}{2XY}\int\int_{\mathcal{D}} \omega dxdy \approx 0.229 \tag{53}$$

or in the dimensional form

$$\Omega_0^* \approx 2.92 \text{ Rad/s} \approx 0.464 \text{ rps}, \quad 1/\Omega_0^* \approx 2.154 \text{ s}. \tag{54}$$

The value of Ω_0 is conserving $(d\Omega_0/dt=0)$ by virtue of Eqs. (46)–(50); it can be presented by the explicit formula

$$\Omega_0 = -\frac{1}{2XY}\int\int_{\mathcal{D}} \Delta\psi dxdy = -\frac{1}{2XY}\int_{\partial\mathcal{D}} \boldsymbol{n}\cdot\nabla\psi dS = -\frac{\mathcal{R}_3\varphi_0}{XY}. \tag{55}$$

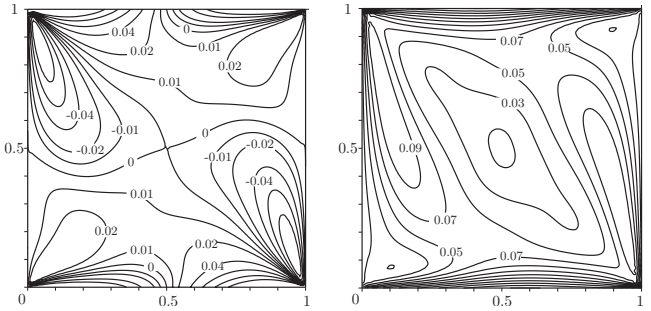

FIG. 8. The isolines of $v_r(x,y,t)$ (left) and $v_\theta(x,y,t)$ at $t=30$.

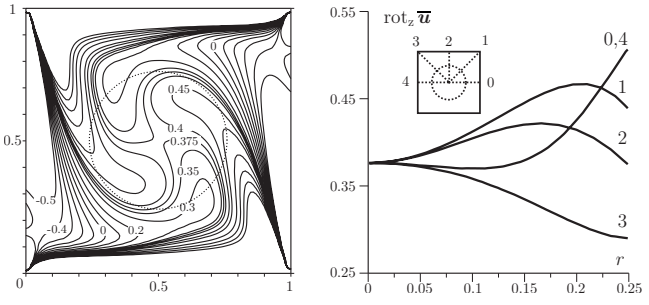

FIG. 9. The isolines of $\omega(x,y,t)$ and $\omega(r,\theta_m,t)$ for $\theta_m=m\pi/4$, $m=0,1,2,3,4$, and $t=30$.

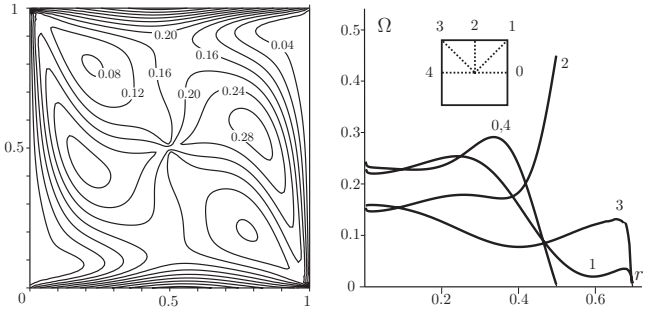

FIG. 10. The isolines of $\Omega(x,y,t)$ and $\Omega(r,\theta_m,t)$ for $\theta_m=m\pi/4$, $m=0,1,2,3,4$, and $t=30$.

Additional computations for the motion of passive admixture (see Sec. VI F) show that the angular velocity of a rotating flow can be better represented not by ω but by the ratio

$$\Omega(x,y,t)=\frac{v_\theta}{r}. \tag{56}$$

The isolines of $\Omega(x,y,t)$ with the step 0.04 are shown in Fig. 10 (left); the right frame shows the graphs of $\Omega(r,\theta_m,t)$ for $0.001<r<0.25$, $\theta_m=m\pi/4$, $m=0,1,2,3,4$, $t=30$ in polar coordinates (r,θ).

The averaged value [defined similarly to Eq. (53)] is

$$\Omega_1=\langle\Omega\rangle=\frac{1}{XY}\int\int_{\mathcal{D}}\Omega dxdy\approx 0.166 \tag{57}$$

or in the dimensional form

$$\Omega_1^*\approx 2.12\ \text{Rad/s}\approx 0.337\ \text{rps},\quad 1/\Omega_1^*\approx 2.966\ \text{s}. \tag{58}$$

The value of Ω_1 for the problem (46)–(50) can be presented by an explicit formula

$$\begin{aligned}\Omega_1&=-\frac{1}{XY}\int\int_{\mathcal{D}}\nabla\psi\cdot\nabla\ln r dxdy\\&=\frac{2\pi}{XY}\int\int_{\mathcal{D}}\psi\delta(\boldsymbol{x}-\boldsymbol{x}_0)dxdy\\&=\frac{2\pi}{XY}\psi_0(\boldsymbol{x}_0,t),\end{aligned} \tag{59}$$

where $\delta(\boldsymbol{x}-\boldsymbol{x}_0)$ is the Dirac delta function, $\boldsymbol{x}_0=(x_0,y_0)$, $x_0=0.5$, and $y_0=0.5$. The calculation of $\psi_0(\boldsymbol{x}_0,t)$ for $t>30$ (when the flow is almost steady, see Fig. 6) yields $\psi_0(\boldsymbol{x}_0,t)\approx 0.02646$, which is in the complete agreement with Eq. (57): $2\pi 0.2646\approx 0.166$, $X=1$, and $Y=1$.

B. Flows in rectangular domains

In addition to the square domain, we perform the computations in rectangular domains with different Y. In all cases $X>Y$, we observe a flow structure similar to the shown in Fig. 6: the initial appearance of two vortices with the subsequent forming of a unified steady rotating flow. For example, the flow for $X=1$ and $Y=0.5$ at the instants $t=7$ (≈ 0.546 s) and $t=30$ (≈ 2.31 s) is shown in Fig. 11.

C. Flows in smoothed square domain

Figure 12 shows the flows in the square domain with the deliberately smoothed angles (the curvature radius is 0.1). One can see that the singularities in the electric field near the vertices do not alter the flow structure. In these computations, we keep the boundary conditions (48)–(50) at $x=0$, X the same, while on the rest of the boundary, we introduce physically similar conditions. In these computations, $\bar{\varphi}=0$ on the part $[A,B]$ of the boundary and $\bar{\varphi}=\varphi_0$ on $[C,D]$. The external electric field acts in the y direction. On the rest of the boundary, the tangential velocity component is proportional to the tangential derivative of the potential [similar to Eq. (49)]. We also keep the no-leak condition valid on the whole boundary.

D. Two-vortex regime in square domain

We have already mentioned that the tangential velocity at the boundary is determined by the relation between the parameters φ_0, E_0, X, and Y [see Eq. (51)] with one possible

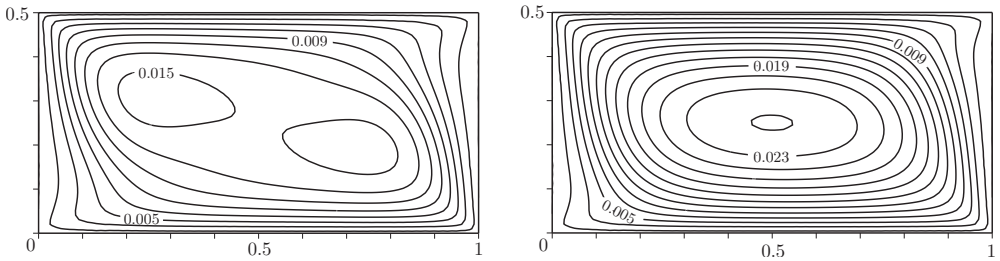

FIG. 11. The streamlines of $\bar{\psi}(x,y,t)$ for $X=1$, $Y=0.5$ at $t=7$ (≈ 0.539 s) and $t=20$ (≈ 1.54 s).

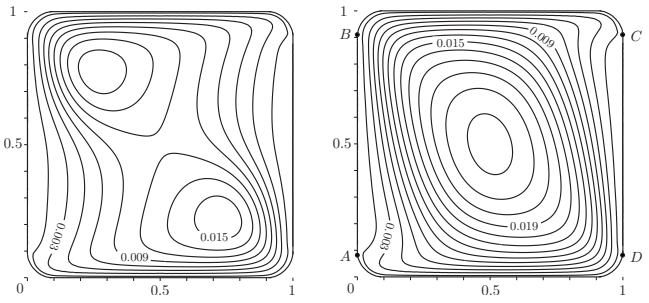

FIG. 12. The streamlines for $\bar{\psi}(x,y,t)$ at $t=10$ (≈ 0.77 s) and $t=30$ (≈ 2.31 s).

flow regime shown in Fig. 4. In order to confirm its existence, we present in Fig. 13 the results for the parameters $\varphi_0=-0.1$, $E_0=0.19$, $X=1$, and $Y=1$. One can see there the isolines of the potential with the step 0.01 and the streamlines at $t=200$ with the step 0.0002. The shown flow regime is almost steady: the norm $\|\bar{\psi}(\cdot,t)\|=0.001\,442$ in the interval $160<t<200$ changes only in the last digit.

In Fig. 13, the tangential velocity at the boundary $y=0$ changes its sign at $x=X_0\approx 0.2$. The computations show that the additional vortices in the angles of the domain do not appear if $X_0\lesssim 0.1$. In particular, for $X=1$, $Y=1$, and $E_0=0.19$, the generation of the rotating flow takes place when $|\varphi_0|>0.6$. It is also interesting to see the differences between the distributions of potentials (cf. Figs. 5 and 13).

E. Square domain with free boundaries at $x=0$, X

Figure 14 shows the results of computations for the same values of parameters but for a different boundary condition when the electrodes represent a free material boundary (see Sec. VA). It is noticeable that in this case, the rotational motion is close to the flow with circular streamlines. This result can be expected physically, since the free slip at the boundaries $x=0$, X does not disturb the flow that is generated by the tangential velocities at the boundaries $y=0$, Y.

Figure 15 shows the isolines of $\Omega(x,y,t)$ with the step 0.1 (left) and the graphs of $\Omega(r,\theta_m,t)$ for $0.001<r<0.25$, $\theta_m=m\pi/4$, $m=0,1,2,3,4$, and $t=30$ in polar coordinates (right) (cf. with Fig. 10). We should notice that Eq. (59) remains valid for the free boundaries, while Eq. (55) fails.

F. On the rotation of fluid

We have already observed that the rotating flows have rather complex structure. The results of Sec. VI A (such as

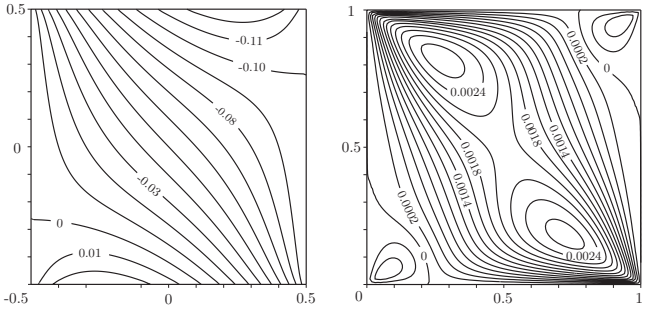

FIG. 13. The isolines of the potential $\bar{\varphi}(x,y)$ (left) and the streamlines for $\bar{\psi}(x,y,t)$ at $t=200\approx 15.4$ s (right).

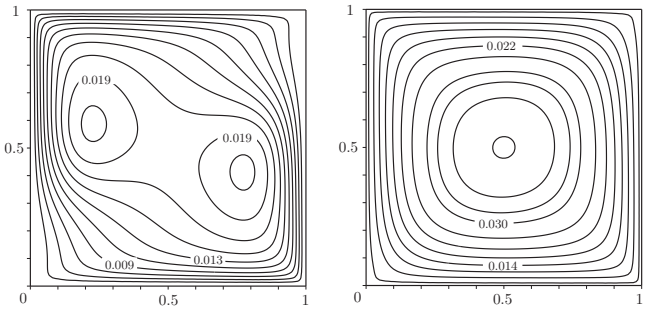

FIG. 14. The streamlines for $\bar{\psi}(x,y,t)$ at $t=10$ (≈ 0.77 s) and $t=30$ (≈ 2.31 s).

presented in Figs. 9 and 10) show that ω and v_θ/r are functions of (x,y). It means that different fluid particles move along the streamlines with different velocities. An instructive flow visualization can be achieved by the placing of a diffusive scalar admixture $c(x,y,t)$ to the flow at the instant t_0 when the flow becomes "almost steady" [55]

$$\frac{\partial c}{\partial t}+\bar{\boldsymbol{u}}(x,y)\nabla_0 c=D_0\Delta_0 c,\quad t>t_0,$$

$$(\boldsymbol{n}\cdot\nabla_0 c)|_{\partial\mathcal{D}}=0,\quad c(x,y,t_0)=c_0(x,y).$$

Figure 16 shows the concentration isolines with the step 0.4 at the instants $t=300$, 500, 700, and 1500 for $D_0=0.0001$, $t_0=30$. It is clearly seen that the concentration distribution taken originally as a "square spot with smoothed angles" undergoes strong deformations and eventually takes the shape that is similar to the streamline geometry (cf. Fig. 16 at $t=1500$ with Fig. 6 at $t=30$).

One can measure the period of rotation of a fluid by observing the concentration at some point (x_n,y_n). Figure 17 shows the time dependence of concentrations $c(x_n,y_n,t)$ for $(x_1=0.7,\ y_1=0.5)$, $(x_1=0.8,\ y_1=0.5)$. Both functions are periodic with the superimposed attenuation due to diffusion. The time interval between the neighboring maxima and minima corresponds to the half of a full revolution (due to the flow symmetry with respect to its rotation over the angle π). The periods of full revolutions are $T_1\approx 36.5$ for (x_1,y_1) and $T_2\approx 33.4$ for (x_2,y_2) that in dimensional terms yield

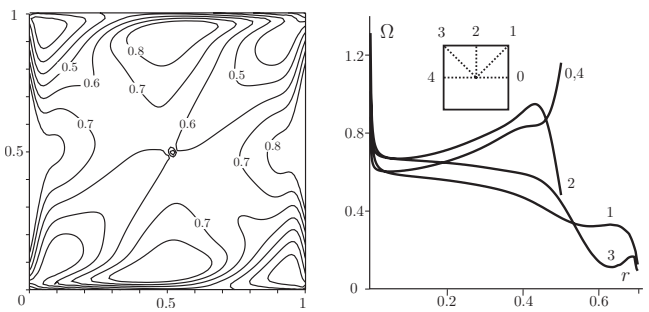

FIG. 15. The isolines of $\Omega(x,y,t)$ and $\Omega(r,\theta_m,t)$ for $\theta_m=m\pi/4$, $m=0,1,2,3,4$, and $t=30$.

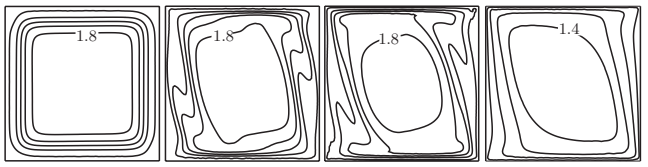

FIG. 16. The isolines of the concentration $c(x,y,t)$ at $t=300$, 500, 700, and 1500.

$$1/T_1^* \approx 0.351 \text{ rps}, \quad 1/T_2^* \approx 0.369 \text{ rps}. \tag{60}$$

These values are close to $\Omega_1^* \approx 0.337$ rps, obtained by the averaging of v_θ/r [see Eqs. (56)–(58)]. It means that the fluid rotation can be better characterized by the averaging of v_θ/r than ω [where $\Omega_0^* \approx 0.464$ rps, see Eqs. (53) and (54)].

Table IV gives the values of angular velocities calculated by the formulas (53) and (57): the first row corresponds to Fig. 6 [see also Eqs. (54), (58), and (60)], the second row corresponds to the free boundaries (see Sec. VI E and Fig. 14), and the third row contains the experimental data of [1–3]. The fourth row gives the results of computations when Navier-Stokes Eqs. (46) are replaced with the Stokes equations (i.e., we drop the term $\bar{\boldsymbol{u}}\cdot\nabla_0\bar{\boldsymbol{u}}$). One can see that the values of angular velocities in the first and fourth rows are close. It indicates that the nonlinearity is small (at least for the computations of the averaged values) and one can try to obtain the analytical solutions in the form of the power series. However, we should notice that during the computations, we observed the different geometries of stream functions for Navier-Stokes and Stokes equations.

Notice that Eq. (55) gives a simple and useful estimation of the angular velocity for the problem (46)–(50). The value of Ω_0 can be found analytically without any use of numerical solution. For the rectangle $[0,a_*]\times[0,b_*]$ it gives

$$\Omega_0^* = -\frac{F_* h_*^4}{135 a_* b_* \rho_*^2 \nu_*^3 \varepsilon_*^2}\left(\frac{2\varepsilon_* c_B^*}{R_* T_*}\right)^{1/2} (\varepsilon_{\text{out}}^* E_{\text{out}}^*)^3 \varphi_0^*. \tag{61}$$

This formula contains the known constants F_*, R_* and three groups of parameters: the first group ρ_*, ν_*, ε_*, c_B^*, and T_* defines the physical properties of the liquid, the second group $\varepsilon_{\text{out}}^*$, E_{out}^*, and φ_0^* determines the external factors, and the third group a_*, b_*, and h_* describes the film geometry; Eq. (61) is valid when

$$\frac{(\varepsilon_{\text{out}}^* E_{\text{out}}^*)^2}{4R_* T_* \varepsilon_* c_B^*} < 0.6, \quad \delta^2 = \frac{h_*^2}{a_*^2} \ll 1,$$

where the first condition appeared during the asymptotic calculation of $\mathcal{R}_3$ [see Eq. (45)] while the second condition represents the main small parameter of our model. It is easy

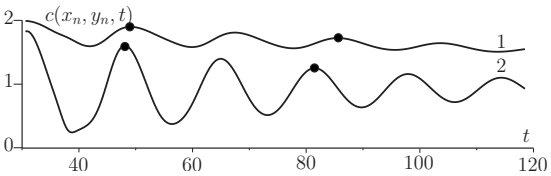

FIG. 17. Concentration $c(x_n,y_n,t)$, $n=1,2$.

TABLE IV. Angular velocities.

No.	Ω_0	$\Omega_0^*\frac{\text{Rad}}{\text{s}}$	Ω_1	$\Omega_1^*\frac{\text{Rad}}{\text{s}}$	$\frac{2\pi}{T_1*}\frac{\text{Rad}}{\text{s}}$
1	0.229	2.975	0.166	2.157	2.200
2	0.739	9.601	0.620	8.0552	8.121
3			$\approx(8-10)\frac{\text{Rad}}{\text{s}}$ [1–3]		
4	0.229	2.975	0.173	2.247	2.603

to check that formula (61) (with the use of the data from Tables I–III) gives the same values of Ω_0^* as in the second and fourth rows of Table IV (the choosing the value h_* is discussed in Sec. VII).

VII. DISCUSSION

The important result of our paper is the formula that links the tangential velocity at the boundary with Reynolds stresses (see Sec. IV). This formula represents the main approximation that can be improved.

Another our main achievement is the explicit formula (61) that predicts the angular velocity of the liquid. It is noticeable that Eq. (61) predicts the rotation of liquid in much broader intervals of parameters than are exploited in the experiments [1–3]. Hence our theory predicts that the phenomenon of the *liquid film motor* can appear in much more general conditions.

The existence of the described rotating EHD flows can be expected since the tangential velocity at the boundaries could generate it. However, it still may look surprising that all considered rotating flows appear as the result of the applying of *constant* fields $\boldsymbol{E}_{\text{out}}$ and φ_0. In this connection, one can also mention the recent paper [56] that describes a EHD plane flow that appears under the action of a constant electric field in the presence of an additional central electrode.

It is interesting to compare our main equations and the used averaging technique to the ones presented in the papers [4–8] devoted to the electrokinetic instability of the EHD flows with inhomogeneous conductivity. The averaged Eqs. (22)–(26) are almost identical to the derived in these papers, although we use different boundary conditions (16)–(19). The Reynolds stresses were also derived in these papers, however, they were neglected due to their smallness. In our model (22)–(26), the situation is right opposite since Reynolds stresses generate a tangential velocity near the boundaries. One can also see in Appendix A that our averaging method is more detailed and transparent than the method of [4–8].

Our model of a rotational flow looks more realistic than the heuristic hypothesis of [1–3] on the changing of the orientations of water molecular dipoles by an external electric field.

The full quantitative comparison of our results to the experiments [1–3] is impossible, since the key information about the values of some crucial parameters is absent in these papers.

The qualitative comparison of our results (Figs. 6, 11, and 12) to the flow pictures in [1–3] shows a good agreement: both in the experiments and in our computations, one can observe the appearance of the rotational flow, growing to its stationary state during the time interval of the order of 2 s. This fact opens the opportunity for the fast switching between the directions of a rotation as has been proposed in [1–3].

There are flows with one vortex and with two vortices in the experiments. According to our computations, only one steady vortex can exist; it appears when the tangential velocity changes its sign at the point $x \lesssim 0.1X$. From another side, we have shown that there are two corotating vortices in the rectangular film with the ratio of sizes 1:2 (that is similar to the experiments). However in our computations, such a flow is not steady, it finally transforms to the flow with single vortex (Fig. 11). However, the authors [1–3] do not mention whether or not the observed flow with two vortices is steady.

The experimental rotating flow appears only for some critical values of the electric field E^*_{out}, which depend on φ^*_0 [1–3]. In particular, the authors of [1–3] indicate that $E^*_{\text{out}}\varphi^*_0$=const for their experiments; using their data, we have estimated that this constant $\approx$500 kV V/m. The rotating flow in our model (46)–(50) also appears only for the certain values of parameters. In particular, data of Table I (for the flows shown in Fig. 6) yield E^*_{out}=30 kV/m, φ^*_0=20 V, so $E^*_{\text{out}}\varphi^*_0$=600 kV V/m. In order to obtain this estimation, one should use Eq. (51) and the comments to Fig. 13.

Experiments [1–3] show that the angular velocity does not depend on the concentration of glycerol in water. However, the formula (61) $\Omega^*_0 \sim (\nu_*)^{-3}(\rho_*)^{-2}(\varepsilon_*)^{-3/2}h^4_*$ contains several parameters that depend on this concentration (one should keep in mind that c^*_B is not the glycerol concentration). Hence, for the verification of Eq. (61), one should directly measure the viscosity, dielectric permeability, density, and the film thickness; all these measurements are not given in [1–3]. At the same time, the theoretical deriving of the dependence of these parameters on the glycerol concentration is very difficult, since the solution of glycerol in water represents a notoriously specific liquid.

The results of [1–3] show that the angular velocity of fluid increases toward the center of a film. On the basis of this fact, the authors of [1–3] deny the electrokinetic effects at the film edges as the possible mechanism that causes the rotation. However, in our model (22)–(26) and in the numerical results (see Figs. 5–12), the fluid is not rotating as a rigid body, it has different angular velocities at different points (see, e.g., Figs. 9 and 10). For example, we first observe a weak growth and then a decrease of Ω along the rays θ=0 and $\theta=\pi$ of the used polar coordinates. At the same time, the angular velocity is growing toward the center along the ray $\theta=\pi/2$. Such a complex behavior looks natural, since the cause of this rotation is the tangential velocity at the boundary [see the boundary conditions (48)]. Also, data of Table IV show that our results strongly depend on the used boundary conditions at x=0, X: the angular velocity in our computations differs from the experiment by the factor of 4 for the no-slip conditions, while for the free boundaries the theory produces a good agreement with the experiments. In order to avoid misunderstandings, we should emphasize that our results strongly depend on the parameters of the problem, especially on the film thickness h_*. A quantitative comparison to the experiment is not feasible now since [1–3] do not contain any data on h_*.

The theoretical evaluation of h_* is difficult. In order to do it, one may consider its following heuristic estimation: let h_* be determined as the additional height of the liquid in a rectangular capillary pipe $h_*=2\sigma_*(a_*+b*)/(\rho_* g_* a_* b*)$, where σ_* is the surface tension and g_* is gravity [57]. Such estimation is based on the imaginary experiment of the pilling up an initially submerged rectangular frame (where both the free surface of liquid and the frame are horizontal). For water $\sigma_* \approx 0.072$ N/m; taking $g_* \approx 9.8$ m^2/s, $a_*=b_* \approx 1.0\times10^{-2}$ m yields the half thickness of the film $h_* \approx 0.29\times10^{-2}$ m. This value has been chosen in the computations of Sec. VI (see Tables I–III). One can expect that this value of h_* corresponds only to the beginning of the experiment; the evaporation (and maybe other factors) makes h_* rapidly decreasing with time. Alternatively, we can also demonstrate the use of formula (61) for the estimation of h_*. Most likely, the parameters used in [1–3] for the measurements of angular velocity are $a_*=b_*=3.1\times10^{-2}$ m, E^*_{out}=60 kV/m, φ^*_0=120 V, $\nu_*=1.3\times10^{-6}$ m^2/s (solution of glycerol), $\varepsilon^*_{\text{out}}=5.0\varepsilon^*_0$ (insulator—textolite). Taking the remaining parameters from Tables I–III yields $h_*=9.48\times10^{-4}$ m (δ=0.03) and $\Omega^*_0 \approx 9.65$ Rad/s (cf. with the third row of Table IV).

Our mathematical model (22)–(33) represents only the simplest asymptotic model of the flow near the boundary. There is a serious potential for the further theoretical developments. Here, one should keep in mind that the modeling of EHD processes in microscales represents a rather complex problem due to the broad spectrum of various physical phenomena such as electrokinetic effects (electro-osmosis, electrophoresis, etc.), the effects of diffusion, the chemical reactions both in a solution and on electrodes, the mass transfer by an electric field, the Joule heat, convection, Taylor-Aris dispersion, etc. In particular, it is unclear whether we have to consider the equilibrium Boltzmann concentrations $c^*_B \approx 10^{-4}$ mol/m^3 or we can have ions of only one sign near the boundaries. We consider as the most sensitive the following three factors. First, our mathematical model is incomplete since it does not consider the surface tension and the deviations of the free surfaces of a film from the planes. Second, our model describes the *averaged* velocity field that differs from the real three-dimensional velocity distribution [see Eq. (A17)]. Due to the accepted electroneutrality of the mixture (almost everywhere except the vicinities of the boundaries), the taking into account the three dimensionality of a flow can produce the decreasing of the rotation for the layers of a film near its boundary. Third, there should be a more complete model to consider the Joule heat that naturally appears in a weakly conductive liquid under the significant electric current (0.2 mA$\times$20 V=4 mW). The resulting nonuniform temperature can cause strong inhomogeneity in viscosity and the permittivity of a solution. We should remind that the changing of temperature from 15 °C to 35 °C produces the changing of water permittivity ε_r from 81.9 to 74.8 ($\partial\varepsilon_r/\partial T \approx 0.35$). For a strong electric field, it can produce a significant pondermotive force $(1/2)\nabla\varepsilon(\nabla\varphi)^2$.

It is especially important to explain the connection between our model and the EDL theories for strong external electric fields [20,27–32]. In our model, the rotating flow is caused by the edge effects at the boundaries $y=0$, Y where simplified boundary conditions lead to the estimation of the value $\mathcal{R}=\mathcal{R}_1(E_0)+\mathcal{R}_3(E_0)$ [Eqs. (49) and (52)]. In doing so, we emphasize the key role of the water-insulator interface and the discovery that the electrokinetic effects can define the relation between $\mathcal{R}_1(E_0)$ and $\mathcal{R}_3(E_0)$. At the same time, this simplified model can be upgraded with the use of contemporary EDL theories. It is a rather complex task that can be undertaken if the industrial applications of the *liquid film motor* appear. Here, one can go ahead with the full solution of the problem that must include the exact evaluation of $\mathcal{R}_1(E_0)$, $\mathcal{R}_3(E_0)$ and the upgrading of the assumption that $E=$const in Eq. (35). For the achieving of such a goal, one should describe the interface flow more precisely, which is possible only with the use of EDL theories. In general, the creation of a full model requires reconsidering or upgrading all results of Sec. IV.

The general significance of our results for the further developments of microhydrodynamics might consist in the revaluation of the roles of the considered classical effects in the micro- and nanoscale processes. In the practical applications, the considered rotating flows can be used for the micromixing in microfluidic devices (see, e.g., Sec. VI F and [58,59]).

ACKNOWLEDGMENTS

This research is supported by EPSRC (Research Grants No. GR/S96616/01, No. EP/D055261/1, and No. EP/D035635/1) as well as by the Russian Ministry of Education (program "Development of the Research Potential of the High School," Grants No. 2.1.1/6095 and No. 2.1.1/554), by Russian Foundation for Basic Research (Grants No. 07-01-00389, No. 08-01-00895, and No. 07-01-92213 PICS), CRDF-RFBR Grant No. 09-01-92504-IK, and Russian-Taiwan Grant No. 95WFE0300007. The authors are grateful to the Department of Mathematics of the University of York for the providing of the excellent conditions for this research.

APPENDIX A: THE AVERAGING PROCEDURE

The averaging of Eqs. (9) and (11)–(14), which takes into account the boundary conditions (16)–(19), gives the exact but not closed system of equations

$$\delta^2(\partial_t\bar{\boldsymbol{u}}+\bar{\boldsymbol{u}}\cdot\nabla_0\bar{\boldsymbol{u}})+\delta^2\,\mathrm{div}_0(\overline{\tilde{\boldsymbol{u}}\otimes\tilde{\boldsymbol{u}}}) = -\delta^2\nabla_0\bar{p}+\delta^2\nu\Delta_0\bar{\boldsymbol{u}}-\bar{q}\nabla_0\bar{\varphi}-\overline{\tilde{q}\nabla_0\tilde{\varphi}}, \tag{A1}$$

$$\mathrm{div}_0\,\bar{\boldsymbol{u}}=0, \tag{A2}$$

$$\varepsilon\Delta_0\bar{\varphi}=-\bar{q}, \tag{A3}$$

$$\partial_t\bar{c}_k+\bar{\boldsymbol{u}}\cdot\nabla_0\bar{c}_k+\mathrm{div}_0(\overline{\tilde{\boldsymbol{u}}\tilde{c}_k})+D_k\,\mathrm{div}_0\,\bar{\boldsymbol{i}}_k=0, \tag{A4}$$

$$\bar{\boldsymbol{i}}_k=-D_k(\nabla_0\bar{c}_k+e_k\gamma\bar{c}_k\nabla_0\bar{\varphi}+e_k\gamma\overline{\tilde{c}_k\nabla_0\tilde{\varphi}}). \tag{A5}$$

In order to obtain the closed system with the precision $O(\delta^4)$, we use the decompositions (21) to calculate the terms

$$\overline{\tilde{\boldsymbol{u}}\otimes\tilde{\boldsymbol{u}}}=\overline{\tilde{\boldsymbol{u}}^0\otimes\tilde{\boldsymbol{u}}^0}+O(\delta^2), \tag{A6}$$

$$\overline{\tilde{q}\nabla_0\tilde{\varphi}}=\overline{(\tilde{q}^0+\delta^2\tilde{q}^1)\nabla_0(\tilde{\varphi}^0+\delta^2\tilde{\varphi}^1)}+O(\delta^4), \tag{A7}$$

$$\overline{\tilde{\boldsymbol{u}}\tilde{c}_k}=\overline{(\tilde{\boldsymbol{u}}^0+\delta^2\tilde{\boldsymbol{u}}^1)(\tilde{c}_k^0+\delta^2\tilde{c}_k^1)}+O(\delta^4), \tag{A8}$$

$$\overline{\tilde{c}_k\nabla_0\tilde{\varphi}}=\overline{(\tilde{c}_k^0+\delta^2\tilde{c}_k^1)\nabla_0(\tilde{\varphi}^0+\delta^2\tilde{\varphi}^1)}+O(\delta^4). \tag{A9}$$

For the main terms in Eq. (21), Eqs. (10) and (12)–(14) and condition (18) yield

$$(\bar{q}^0+\tilde{q}^0)\partial_z\tilde{\varphi}^0=0,\quad \bar{q}^0+\tilde{q}^0=\sum_k e_k(\bar{c}_k^0+\tilde{c}_k^0), \tag{A10}$$

$$\partial_z\bar{I}_k^0=0,\quad \bar{I}_k^0+\tilde{I}_k^0=\partial_z\tilde{c}_k^0+e_k\gamma(\bar{c}_k^0+\tilde{c}_k^0)\partial_z\tilde{\varphi}^0,$$

$$(\bar{I}_k^0+\tilde{I}_k^0)|_{z=\pm1}=0. \tag{A11}$$

Equations (A10) and (A11) give $\partial_z\tilde{\varphi}^0=0$, $\partial_z\tilde{I}_k^0=0$, and $\tilde{I}_k^0=\partial_z\tilde{c}_k^0$. It is clear that if $\partial_z\tilde{f}=0$, then $\tilde{f}=0$ and $f=\bar{f}$. Hence

$$\tilde{\varphi}^0=0,\quad \tilde{c}_k^0=0,\quad \tilde{q}^0=0,$$

$$\varphi^0=\bar{\varphi}^0,\quad c_k^0=\bar{c}_k^0,\quad q^0=\bar{q}^0. \tag{A12}$$

The use of Eq. (A12) transforms the expressions (A7)–(A9) to the form

$$\overline{\tilde{q}\nabla_0\tilde{\varphi}}=O(\delta^4),$$

$$\overline{\tilde{\boldsymbol{u}}\tilde{c}_k}=\delta^2\overline{\tilde{\boldsymbol{u}}^0\tilde{c}_k^1}+O(\delta^4),\quad \overline{\tilde{c}_k\nabla_0\tilde{\varphi}}=O(\delta^4). \tag{A13}$$

From Eqs. (9) and (A12), we obtain the equation for $\tilde{\boldsymbol{u}}^0$,

$$\nu\partial_{zz}\tilde{\boldsymbol{u}}^0-\bar{q}^0\nabla_0\bar{\varphi}^0=0,$$

which is required for the calculation of Eq. (A6) with the precision $O(\delta^2)$. In particular, it means that we can make the replacements $\bar{q}=\bar{q}^0+O(\delta^2)$, $\bar{\varphi}=\bar{\varphi}^0+O(\delta^2)$ and $\tilde{w}_0$, $\tilde{\boldsymbol{u}}_0$ can be found from the equations

$$\nu\partial_{zz}\tilde{\boldsymbol{u}}^0-\bar{q}\nabla_0\bar{\varphi}=0, \tag{A14}$$

$$\mathrm{div}_0(\bar{\boldsymbol{u}}^0+\tilde{\boldsymbol{u}}^0)+\partial_z\tilde{w}^0=0, \tag{A15}$$

with the boundary condition

$$\bar{w}^0+\tilde{w}^0=0,\quad z=\pm1. \tag{A16}$$

We assume that $\bar{w}^0=0$. The integration of Eqs. (A14)–(A16) yields

$$\tilde{\boldsymbol{u}}^0=g'(z)\boldsymbol{U},\quad \tilde{w}^0=-g(z)\mathrm{div}_0\,\boldsymbol{U},\quad \nu\boldsymbol{U}=\bar{q}\nabla_0\bar{\varphi},$$

$$\mathrm{div}_0\,\bar{\boldsymbol{u}}^0=0,\quad g(z)=\frac{1}{6}(z^3-z),\quad \overline{g(z)}=0,\quad \overline{g'(z)}=0, \tag{A17}$$

where we have used the notation Eq. (26) for $\boldsymbol{U}$.

One can notice that we do not require $\tilde{\boldsymbol{u}}^0$ to satisfy the boundary condition (17). This condition is required only for

$\tilde{\boldsymbol{u}}$. The equality $\partial_z \tilde{\boldsymbol{u}}^0 = 0$ at $z = \pm 1$ leads to $\boldsymbol{U} = 0$ that is not true. In an exact problem, one should consider a boundary-layer solution at $z = \pm 1$ and assume the absence of a charge ($\bar{q} = 0$) at the boundary. If it is not accepted, then the action of a tangential to the boundary external field creates the stresses related to the electromagnetic stress tensor.

The use of Eq. (A17) gives the expression for Eq. (A6)

$$\overline{\tilde{\boldsymbol{u}} \otimes \tilde{\boldsymbol{u}}} = \overline{g'^2(z)}(\boldsymbol{U} \otimes \boldsymbol{U}) + O(\delta^2), \quad \overline{g'^2(z)} = \frac{1}{45}. \tag{A18}$$

The calculation of $\overline{\tilde{\boldsymbol{u}}\tilde{c}_k}$ is based on the next approximation for the Eqs. (12)–(14)

$$\partial_t c_k^0 + \boldsymbol{u}^0 \cdot \nabla_0 c_k^0 + w^0 \partial_z c_k^0 + \mathrm{div}_0\, \boldsymbol{i}_k^0 + \partial_z I_k^1 = 0,$$

$$\boldsymbol{i}_k^0 = -D_k(\nabla_0 c_k^0 + e_k \gamma c_k^0 \nabla_0 \varphi^0),$$

$$I_k^1 = -D_k[\partial_z c_k^1 + e_k \gamma (c_k^1 \partial_z \varphi^0 + c_k^0 \partial_z \varphi^1)],$$

$$\varepsilon(\Delta_0 \varphi^0 + \partial_{zz} \varphi^1) = -q^0$$

or taking in account Eq. (A12)

$$\partial_t \bar{c}_k^0 + (\bar{\boldsymbol{u}}^0 + \tilde{\boldsymbol{u}}^0) \cdot \nabla_0 \bar{c}_k^0 + \mathrm{div}_0\, \boldsymbol{i}_k^0 + \partial_z I_k^1 = 0,$$

$$\boldsymbol{i}_k^0 = -D_k(\nabla_0 \bar{c}_k^0 + e_k \gamma \bar{c}_k^0 \nabla_0 \bar{\varphi}^0),$$

$$I_k^1 = -D_k(\partial_z \tilde{c}_k^1 + e_k \gamma \bar{c}_k^0 \partial_z \tilde{\varphi}^1),$$

$$\varepsilon(\Delta_0 \bar{\varphi}^0 + \partial_{zz} \bar{\varphi}^1) = -\bar{q}^0. \tag{A19}$$

The last equation shows that $\partial_{zz}\bar{\varphi}^1$ does not depend on z, so to find $\tilde{c}_k^1$, we obtain the equation

$$\tilde{\boldsymbol{u}}^0 \cdot \nabla_0 \bar{c}_k^0 - D_k \partial_{zz} \tilde{c}_k^1 = 0, \tag{A20}$$

with the boundary conditions that follow from Eq. (18)

$$\partial_z \tilde{c}_k^1|_{z=\pm 1} = 0.$$

For the calculation of $\overline{\tilde{\boldsymbol{u}}\tilde{c}_k}$, one can take $\bar{c}_k = \bar{c}_k^0 + O(\delta^2)$ in Eq. (A20) since the required precision for Eq. (A8) is $O(\delta^2)$. It allows us to integrate Eq. (A20)

$$D_k \tilde{c}_k^1 = [g_0(z) - \overline{g_0(z)}]\boldsymbol{U} \cdot \nabla_0 \bar{c}_k, \quad g_0(z) = \frac{z^2}{12}\left(\frac{1}{2}z^2 - 1\right).$$

Finally, we obtain

$$\overline{\tilde{\boldsymbol{u}}^0 \tilde{c}_k^1} = -\alpha_k \boldsymbol{U}(\boldsymbol{U} \cdot \nabla_0 \bar{c}_k),$$

$$\alpha_k = -\frac{1}{D_k}\{\overline{g'(z)[g_0(z) - \overline{g_0(z)}]}\} = \frac{4}{945 D_k}. \tag{A21}$$

APPENDIX B

Let us show that in the case (35), Eq. (22) can be integrated. The use of Eqs. (42) and (26) gives us the velocity component $\bar{u}$,

$$\frac{\beta}{\nu^2} E \partial_y(\bar{q}^2 \partial_y \Phi) = -\delta^2 \partial_x p + \nu \delta^2 \partial_{yy} \bar{u} - \bar{q} E. \tag{B1}$$

Taking in account that $\bar{q}$, Φ, and $\bar{u}$ depend only on y, we get

$$-\delta^2 p = \left\{\frac{\beta}{\nu^2} E \partial_y(\bar{q}^2 \partial_y \Phi) - \nu \delta^2 \partial_{yy} \bar{u} + \bar{q} E\right\} x + H(y).$$

Its substitution into the Eq. (22) for w shows that p depends only on y,

$$\frac{\beta}{\nu^2} \partial_y(\bar{q} \partial_y \Phi)^2 + \bar{q} \partial_y \Phi = H'(y).$$

It follows that the expression in braces is vanishing and Eq. (B1) gives us Eq. (43).

APPENDIX C

Let us consider the case when the values of all diffusion coefficients are the same ($D_k \equiv D$). The multiplying of Eq. (A4) by e_k and combining the results yield

$$\frac{d\bar{q}}{dt} + \mathrm{div}_0(\overline{\tilde{\boldsymbol{u}}\tilde{q}}) - D\, \mathrm{div}_0(\nabla_0 \bar{q} + \sigma \nabla_0 \bar{\varphi}) = 0,$$

where $\sigma = D\Sigma_k e_k^2 \gamma \bar{c}_k$ is the conductivity of a mixture. We have also taken Eq. (A21) into account. By virtue of Eq. (A21), the electroneutrality $\bar{q} = 0$ leads to $\tilde{q} = 0$ everywhere except the boundaries. Hence, in the case $\bar{c}_k = c_B$ [see Eq. (37)], we arrive to Eq. (47).

The requirement of the equality of all diffusion coefficients represents a strong restriction. In particular, the difference between the diffusion coefficients leads to the electrokinetic instabilities due to the term $\overline{\tilde{\boldsymbol{u}}\tilde{q}}$ that is linked to the Taylor-Aris dispersion [4–8].

[1] R. Shirsavar, A. Amjadi, N. Hamedani Radja, M. D. Niry, M. Reza Rahimi Tabar, and M. R. Ejtehadi, e-print arXiv:cond-mat/0605029.

[2] A. Amjadi, R. Shirsavar, N. Hamedani Radja, and M. R. Ejtehadi, e-print arXiv:0805.0490.

[3] A. Amjadi, R. Shirsavar, N. Hamedani Radja, and M. R. Ejtehadi, Microfluid. Nanofluid. **6**, 711 (2009).

[4] M. H. Oddy and J. G. Santiago, Phys. Fluids **17**, 064108 (2005).

[5] B. D. Storey, B. S. Tilley, H. Lin, and J. G. Santiago, Phys. Fluids **17**, 018103 (2005).

[6] C.-H. Chen, H. Lin, S. K. Lele, and J. G. Santiago, J. Fluid Mech. **524**, 263 (2005).

[7] H. Lin, B. D. Storey, and J. G. Santiago, J. Fluid Mech. **608**, 43 (2008).

[8] H. Lin, B. D. Storey, M. H. Oddy, Ch.-H. Chen, and J. G.

Santiago, Phys. Fluids **16**, 1922 (2004).
[9] J. C. Baygents and F. Baldessari, Phys. Fluids **10**, 301 (1998).
[10] H.-K. Yeoh, Q. Xu, and O. A. Basaran, Phys. Fluids **19**, 114111 (2007).
[11] B. S. Tilley, P. G. Petropoulos, and D. T. Papageorgioua, Phys. Fluids **13**, 3547 (2001).
[12] D. Tseluiko, M. G. Blyth, D. T. Papageorgiou, and J.-M. Vanden-Broeck, Phys. Fluids **20**, 042103 (2008).
[13] N. A. Mortensen, L. H. Olesen, L. Belmon, and H. Bruus, Phys. Rev. E **71**, 056306 (2005).
[14] K. T. Chu and M. Z. Bazant, J. Colloid Interface Sci. **315**, 319 (2007).
[15] Z. G. Chiragwandi, O. Nur, M. Willander, and I. Panas, Appl. Phys. Lett. **87**, 153109 (2005).
[16] V. B. Deyirmenjian, Z. A. Daya, and S. W. Morris, e-print arXiv:patt-sol/9703001.
[17] J. R. Melcher and G. I. Taylor, Annu. Rev. Fluid Mech. **1**, 111 (1969).
[18] R. M. Ehrlich and J. R. Melcher, Phys. Fluids **25**, 1785 (1982).
[19] D. A. Saville, Annu. Rev. Fluid Mech. **29**, 27 (1997).
[20] B. Zaltzman and I. Rubinstein, J. Fluid Mech. **579**, 173 (2007).
[21] M. S. Kilic and M. Z. Bazant, e-print arXiv:0712.0453.
[22] M. Z. Bazant, K. Thornton, and A. Ajdari, Phys. Rev. E **70**, 021506 (2004).
[23] A. Ajdari, Phys. Rev. E **53**, 4996 (1996).
[24] A. Ajdari, Phys. Rev. Lett. **75**, 755 (1995).
[25] A. Ajdari, Phys. Rev. E **65**, 016301 (2001).
[26] J. G. Santiago, Anal. Chem. **73**, 2353 (2001).
[27] M. S. Kilic, M. Z. Bazant, and A. Ajdari, Phys. Rev. E **75**, 021502 (2007).
[28] B. D. Storey, L. R. Edwards, M. S. Kilic, and M. Z. Bazant, Phys. Rev. E **77**, 036317 (2008).
[29] M. S. Kilic, M. Z. Bazant, and A. Ajdari, Phys. Rev. E **75**, 021503 (2007).
[30] K. T. Chu and M. Z. Bazant, e-print arXiv:physics/0406076.
[31] M. Z. Bazant, K. T. Chu, and B. J. Bayly, e-print arXiv:physics/0406075.
[32] S. S. Dukhin, R. Zimmermann, and C. Werner, Colloids Surf., A **195**, 103 (2001).
[33] T. M. Squires and S. R. Quake, Rev. Mod. Phys. **77**, 977 (2005).
[34] H. A. Stone, A. D. Stroock, and A. Ajdari, Annu. Rev. Fluid Mech. **36**, 381 (2004).
[35] D. Erickson and D. Li, Langmuir **19**, 5421 (2003).
[36] S. V. Ermakov, S. C. Jacobson, and J. M. Ramsey, Anal. Chem. **70**, 4494 (1998).
[37] S. V. Ermakov, S. C. Jacobson, and J. M. Ramsey, Anal. Chem. **72**, 3512 (2000).
[38] Y. Hu, C. Werner, and D. Li, Anal. Chem. **75**, 5747 (2003).
[39] S. Pennathur and J. G. Santiago, Anal. Chem. **77**, 6772 (2005).
[40] J. D. Posner and J. G. Santiago, J. Fluid Mech. **555**, 1 (2006).
[41] D. Kaniansky, M. Masár, R. Bodor, M. Zuborova, E. Ölvecká, M. Jöhnck, and B. Stanislawski, Electrophoresis **24**, 2208 (2003).
[42] R. Bharadwaj, J. G. Santiago, and B. Mohammadi, Electrophoresis **23**, 2729 (2002).
[43] J. I. Molho, A. E. Herr, B. P. Mosier, J. G. Santiago, and Th. W. Kenny, Anal. Chem. **73**, 1350 (2001).
[44] C. Jen, C. Wu, Y. Lin, and C. Wu, Lab Chip **3**, 77 (2003).
[45] T. J. Johnson, D. Ross, and L. E. Locascio, Anal. Chem. **74**, 45 (2002).
[46] M. H. Oddy, J. G. Santiago, and J. C. Mikkelsen Anal. Chem. **73**, 5822 (2001).
[47] D. Laser and J. G. Santiago, J. Micromech. Microeng. **14**, R35 (2004).
[48] L. D. Landau and E. M. Lifshitz, *Electrodynamics of Continuous Media* (Pergamon Press, Oxford, 1985).
[49] J. D. Jackson, *Classical Electrodynamics* (Wiley, New York, 1963).
[50] S. S. Dukhin and B. V. Deryagin, *Electrophoresis* (Nauka, Moscow, 1976) (In Russian).
[51] A. M. Ilin, *Matching of Asymptotic Expansions of Solutions of Boundary Value Problems* (American Mathematical Society, Providence, 1992).
[52] A. Chorin, J. Comput. Phys. **2**, 12 (1967).
[53] R. Rannacher, in *Navier-Stokes Equations: Theory and Numerical Methods*, edited by R. Rautmann *et al.*, Proceedings of the Oberwolfach Conference 1991 (Springer, New York, 1992).
[54] F. Hecht, O. Pironneau, A. Le Hyaric, and K. Ohtsuka, FREEFEM++ Manual http://www.freefem.org/ff++.
[55] Of course, it would be better to consider the advection of passive admixture without any diffusion. However, such a hyperbolic problem requires special numerical methods. Moreover, the computations anyway produce a computational diffusion.
[56] M. M. Gregersen, M. B. Andersen, G. Soni, C. Meinhart, and H. Bruus, Phys. Rev. E **79**, 066316 (2009).
[57] The classical formula for a circular capillary tube of diameter d_* is $h_*=4\sigma_*/(\rho_* g_* d_*)$.
[58] G. Karniadakis, A. Beskok, and N. Aluru, *Microflows and Nanoflows. Fundamentals and Simulation*, Interdisciplinary Applied Mathematics Vol. 29 (Springer Science, New York, 2005).
[59] C.-C. Chang and R.-J. Yang, Phys. Fluids **21**, 052004 (2009).